THE ASTROPHYSICAL JOURNAL, 527:1009–1022, 1999 December 20

THE NEAR-INFRARED SKY EMISSION AT THE SOUTH POLE IN WINTER

A. PHILLIPS, M. G. BURTON, M. C. B. ASHLEY, J. W. V. STOREY, AND J. P. LLOYD[1,2]
School of Physics, University of New South Wales, Sydney, NSW, Australia 2052
D. A. HARPER
University of Chicago, Yerkes Observatory, Williams Bay, Wisconsin 53191
AND
J. BALLY
Department of Atmospheric, Planetary, and Astrophysical Sciences, University of Colorado, Boulder, Colorado 80309-0391
Received 1998 November 23; accepted 1999 August 5

ABSTRACT

The Antarctic plateau provides superb sites for infrared astronomy, a result of the combination of low temperatures, low levels of precipitable water vapor, high altitude, and atmospheric stability. We have undertaken measurements of the sky background from 1 to 5 μm at the South Pole, using a single channel InSb spectrometer, the Infrared Photometer Spectrometer (IRPS), during the winter (dark) period of 1995. The IRPS records the DC level of the sky flux through a 4° beam and a variety of broadband and narrowband (1%) filters. It can be scanned in elevation from horizon to horizon through the zenith. We find a 20–100 times reduction in the background of thermal emission compared to that from mid-latitude sites such as Siding Spring and Mauna Kea, with typical background levels of 80–200 μJy arcsec^{-2} at 2.43 μm, 100–300 mJy arcsec^{-2} at 3.6 μm and $\sim$0.5 Jy arcsec^{-2} at 4.8 μm. Airglow emission contributes significantly to the sky flux shortward of $\sim$2.4 μm, which is why the $K_{\rm dark}$ (2.27–2.45 μm) band emission does not drop to the 10–20 μJy arcsec^{-2} levels originally predicted. The darkest window for IR observations from the South Pole is from 2.35 to 2.45 μm, where the fluxes from the atmosphere may drop to as low as $\sim$50 μJy arcsec^{-2} at times. Airglow dominates the emission at J (1.25 μm) and H (1.65 μm), but the flux levels of 300–600 μJy arcsec^{-2} and 800–2000 μJy arcsec^{-2}, respectively, are also one-third to one-half those at temperate sites. We find no evidence for any significant contribution from auroral emission to the $K_{\rm dark}$ band. During twilight, when the Sun is $<10°$ below the horizon, scattered sunlight contributes to the sky background with a Rayleigh-type spectrum. Scattered moonlight is also evident in the sky emission at the J band when the Moon is up.

Subject headings: atmospheric effects — infrared: general — instrumentation: photometers — radiation mechanisms: thermal — radiative transfer

1. INTRODUCTION

Ground-based infrared astronomy for wavelengths longer than 2.2 μm is limited by the thermal background from the telescope and the atmosphere above an observing site. Low temperature, low emissivity, and high stability in the atmosphere all combine to produce the most sensitive observing conditions, and nowhere is this more so than on the Antarctic plateau (Burton et al. 1994). Wintertime temperatures drop below $-60°$ C, the column of precipitable water vapor can fall below 250 μm, and there are extended periods of stable weather with no diurnal cycle. As measured by Ashley et al. (1996) and Nguyen et al. (1996), the background at 2.4 μm (a wavelength at which both thermal and airglow emission are minimal) at the South Pole can drop to 100 μJy arcsec^{-2}, or $\sim$50 times less than at typical temperate sites. Broadband observations at this wavelength would be several magnitudes more sensitive than if undertaken with the same facility at a temperate site.

However, while determining the sky background above the Antarctic plateau in this "$K_{\rm dark}$" window (2.27–2.45 μm) provided the motivation for astronomical site testing at the South Pole, it has become apparent that more significant gains may be achieved at slightly longer wavelengths, in the true thermal infrared. For instance, in the 3–4 μm L-band window, while the reduction in thermal background is less than at 2.4 μm, the gain is achieved across the entire window, unlike in the 2.0–2.4 μm K window where it occurs only at the long-wavelength end. Furthermore, in the L band there is new scientific focus, particularly in the study of the embedded population of star-forming regions and searches for the signatures of protostellar disks (e.g., Burton, Storey, & Ashley 1999).

There is thus great interest in extending the site testing at the South Pole to thermal IR wavelengths. To this end we have obtained further observations using the Infrared Photometer Spectrometer (IRPS; Ashley et al. 1995), collecting an extensive data set on the site conditions across the near-IR windows from 1 to 5 μm. We report these data here. They include both broad- and narrowband measurements of the zenith sky intensity and its variation with zenith angle. In addition, these data provide a wealth of information on other site conditions, such as auroral emission, airglow emission, cloud cover, and the length of twilight, as a function of wavelength. We are also measuring the site conditions at other wavelengths, using an automated observatory (the Automated Astrophysical Site Testing Observatory [AASTO]; see Storey, Ashley, & Burton 1996). In particular, results for the mid-infrared windows, from 5 to 15 μm, are reported in Chamberlain et al. (1999). Other papers published on the infrared sky brightness at the Pole include Smith & Harper (1998) and Ashley (1998). Results on the site seeing have been presented by Marks et al. (1996), Marks et al. (1999), and Loewenstein et al. (1998).

[1] University of Chicago, Yerkes Observatory.
[2] Present address: University of California, Berkeley.

A summary of South Pole site characteristics is given by Burton (1998).

We describe the instrument and the measurements made in § 2. The theory behind the analysis of skydips is provided in § 3, the effects of cloud, the Sun, and the Moon on the data in § 4, and our results for the sky backgrounds across the near-IR windows in § 5. These are compared with other sites in § 6, and conclusions are drawn in § 7.

2. EXPERIMENTAL METHOD

2.1. *Instrument*

A single-channel 1–5 μm InSb photometer, the Infrared Photometer Spectrometer (IRPS), placed on top of the Martin A. Pomerantz Observatory (MAPO) building at the South Pole, was used for these observations. This instrument was previously employed on the Anglo-Australian Telescope (AAT) from 1980 to 1992 and allows a direct measure of the sky flux without the need for chopping (Barton & Allen 1980; Allen 1981). Inside are a series of broadband filters (J [1.08–1.32 μm], H [1.51–1.79], K [1.99–2.41 μm], 2.3 μm [2.22–2.41 μm], and M [4.6–5.0 μm]) and two 1% circular variable filters (CVFs) covering the wavelength ranges 1.4–2.5 μm and 2.9–4.2 μm. The 2.3 μm filter has been added since the 1994 South Pole measurements (Ashley et al. 1996) in order to provide broadband data in the darkest part of the sky spectrum. While not quite optimum for measuring the $K_{\rm dark}$ 2.27–2.45 μm window (where airglow emission is predicted to be a minimum), it provides a good measure of its level. We thus often refer to measurements made through the 2.3 μm filter as "$K_{\rm dark}$" in this paper.

All filters can be used through a variety of apertures, and the detector, optics, and filters are cooled to $\sim$65 K with solid nitrogen. An external rotatable flat mirror allows the instrument to function as a stand-alone telescope, able to observe from horizon to horizon along a fixed meridian (20°–200°) through a 3°.8 beam and with an effective collecting area of a few square millimeters (set by an aperture whose diameter can be varied between 0.4 and 5 mm). A full description of the instrument, including all the modifications necessary for remote operation at ambient temperatures down to $-80°$ C, is given in Ashley et al. (1995) and Ashley et al. (1996).

Operation of the instrument is via a series of software macros that can control the filter, aperture, and mirror positions and the integration time. These macros are sent via electronic mail to a Unix workstation at the Pole that communicates directly with the IRPS control computer over the local ethernet. The data is automatically transferred back to Sydney over the Internet after completion of each macro.

2.2. *Observations*

The measurements consisted of the series of skydips and spectral measurements listed in Table 1. Each sequence took 2 hr to complete. In total, we obtained 881 sequences sampling a wide range of observing conditions from clear sky to fog between 1995 May and September (from day-of-year [DOY] 147–261), including into the bright twilight just before sunrise. Apart from a few periods of downtime associated with instrumental problems, the instrument ran continuously during this time, without regard to weather conditions.

Spectra were obtained by scanning the CVF in steps of $\Delta\lambda/\lambda = 0.5\%$ (half the spectral resolution) across the H–K (1.4–2.5 μm) and L (2.9–4.2 μm) bands, at two zenith angles, overhead and at $\pm 76°.5$. Typical zenith spectra are presented in Figure 1.

Skydips were obtained at the fixed filter positions (J, H, K, 2.3 μm, M and at 2.43 μm on the CVF) by scanning the rotating mirror from horizon to horizon, through the zenith, in steps of 4°.5.

Flux calibration for wavelengths beyond 2 μm was determined by observations of blackbodies at 0° and 60° C in 1995 February and 1996 February. The two calibrations were consistent within 5%. Assuming an estimated uncertainty in the temperature of $\pm 1°$ yields an overall uncertainty in flux of $\pm 10\%$. For wavelengths shortward of 2 μm observations of astronomical sources provided a calibration for the broadband filters (as described in § 2.3). At these wavelengths we estimate the accuracy is only 30%–40%. Observations of astronomical sources also provided an independent confirmation of the blackbody calibration from 2 to 2.5 μm. For the CVF spectra shortward of 2.1 μm no direct flux calibration measurements could be made, so we applied a notional calibration factor equal to that at 2.1 μm. This may be wrong by up to 20%–30% in the H band.

We estimate that the contribution to the measured fluxes from thermal emission of the IRPS (principally the mirror, heated a few degrees above ambient) will be small at K and L, but significant at M. For example, a mirror at $-55°$ C with 5% emissivity would add a flux of 4 μJy arcsec^{-2} at 2.4 μm, 25 mJy arcsec^{-2} at 3.8 μm and 0.5 Jy arcsec^{-2} at 4.8 μm, the last flux being of the same order of magnitude as that measured for the sky.

TABLE 1

OBSERVING SEQUENCE

Filter	Wavelength (μm)	Bandpass (μm)	Rotator Angle (step) (deg)	Aperture (mm)	Gain	Integration Time (s)
J	1.25	0.24	−90→90(4.5)	1.0	1000	1.2
H	1.65	0.28	−90→90(4.5)	1.0	1000	1.2
K	2.2	0.42	−90→90(4.5)	1.0	1000	1.2
2.3 μm	2.3	0.19	−90→90(4.5)	2.8	1000	1.2
M	4.6	0.4	−90→90(4.5)	0.4	1	1.2
HK CVF	2.43	0.02	−90→90(4.5)	1.4 × 3.0	1000	1.2
HK CVF	1.4–2.5	λ/100	0, ±76.5	1.4 × 3.0	1000	1.2
L CVF	2.9–4.1	λ/100	0, ±76.5	1.0	1	1.2

NOTE.—Sequence of filter/CVF positions, together with rotator angles, aperture sizes, gains, and integration times used in the observing macro.

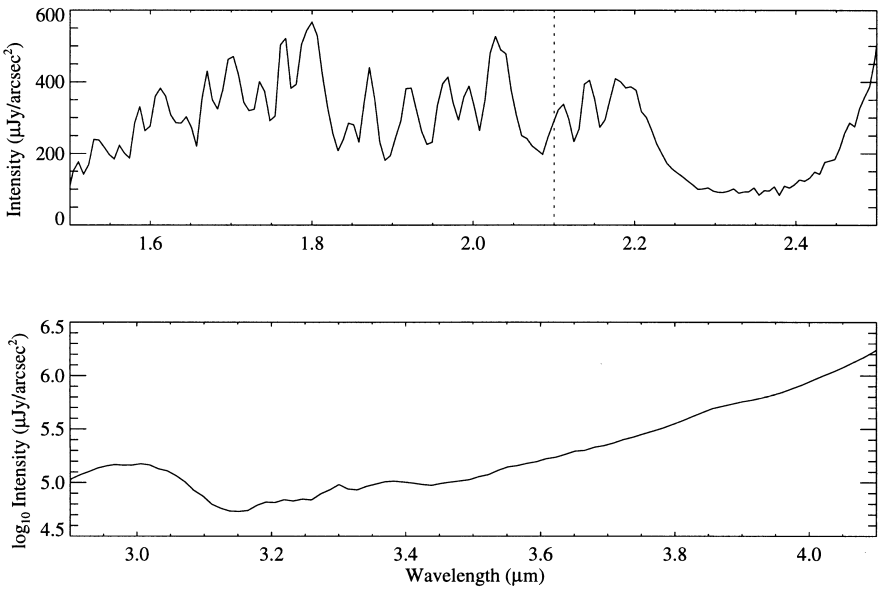

FIG. 1.—Sky emission above the South Pole in μJy arcsec^{-2}, from (*upper panel*) 1.5 to 2.5 μm and (*lower panel*) from 2.9 to 4.1 μm, obtained with 1% spectral resolution through the IRPS CVF. These are the median of all the darkest-sky spectra (i.e., of the darkest 20% of the data) obtained during the winter of 1995. Note that the upper plot uses a linear, and the lower plot a log, intensity scale. For wavelengths less than 2.1 μm (*dashed line*), the data use a nominal calibration factor (see text).

2.2.1. *Skydips*

Skydip scans could be contaminated by emission from clouds and from twilight. As described in § 4 (and summarized in Table 2) this had to be identified and any affected scans removed from the analysis. Figure 2 shows darkest-sky skydip profiles for the IRPS fixed-filter wavebands. These were formed from the median of the darkest 20% of the dark-sky profiles, after each was normalized to a zenith intensity of unity. For reference the secant of the zenith angle, or air mass, is also included. A bump in some of the skydip curves at about $z = 30°$ is due to the Galactic plane (although it is not apparent in the median). This could be seen in all bands except M, where it is overwhelmed by thermal emission from the atmosphere. The M-band (4.8 μm) data contain a significant instrumental DC component, flattening the shape of the skydip curve.

Figure 3 presents the calibrated skydip curves through these same filters. Figure 4 shows an examples of $K_{\rm dark}$ skydip profiles passing through the star R Doradus (a variable star with a mean K-band magnitude ~ -3.8) and the Galactic plane. As is apparent, such bright stars are easily identified. At the Pole, a skydip scan passing through R Doradus (R.A. $4^{\rm h}37^{\rm m}$) will also slice though the Galactic plane along a line of R.A. = $16^{\rm h}37^{\rm m}$, as can readily be seen on the right-hand side of the upper figure. Since in $K_{\rm dark}$ the Galaxy is bright relative to the sky emission and extends over a large angle, it could be mistaken for cloud. Selection for cloud-free data was careful to account for the expected Galactic brightness. This is especially apparent in the lower figure, where the skydip tracks along R.A. = $5^{\rm h}45^{\rm m}/17^{\rm h}45^{\rm m}$, passing through the Galactic center.

TABLE 2

ACCEPTANCE CRITERIA

Acceptance Criteria	Data Remaining (%)
All data (881 records)	100
Detector < 75 K	86
Solar elevation $z > 100°$	63
Zenith intensity 0–400 times normal	62
Skydip curve symmetry	55

NOTE.—Summary of acceptance criteria for selecting data suitable for dark-sky analysis. The data that pass all these criteria (i.e., 55% of the total) we refer to as the "dark-sky" data. However possibly as many as one-half of these may have some residual contributions from cloud somewhere in the skydip.

2.3. *Comparison with DIRBE*

The *COBE* satellite included the Diffuse Infrared Background Experiment (DIRBE). During 1989–1990 this instrument mapped the entire sky at 10 infrared wavelengths from 1.25 to 240 μm, with an angular resolution of ~0.°6 (Hauser et al. 1998). These maps provide an additional flux calibration for the IRPS. The South Pole atmo-

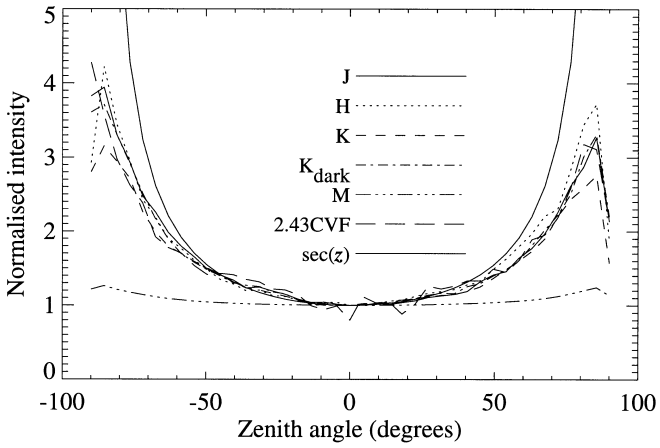

FIG. 2.—Darkest-sky skydips (median of the darkest 20% of the dark-sky data), normalized to a zenith intensity of unity. The variation of sec z, or airmass curve, is shown for reference. The M-band data contain a significant instrumental DC component.

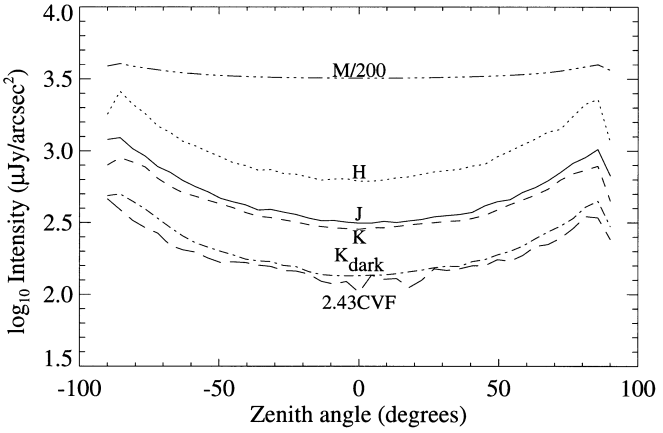

FIG. 3.—IRPS median skydip curves calibrated in units of μJy arcsec^{-2} through the six filters (J, H, K, K_{dark} [2.3 μm], 2.43 μm CVF, and M) used. Note that the M-band data have been divided by a factor of 200.

spheric emission in the infrared K_{dark} band is so low that the plane of the Galaxy and several bright stars are clearly observed by the IRPS, as is apparent in Figure 4. The IRPS had a fixed orientation, and from the time of a skydip the position of the beam on the celestial sphere can be determined. With sufficient scans a map of the sky can be formed and directly compared to the DIRBE sky map. Figure 5*a* shows the DIRBE 2.2 μm sky map with resolution smoothed to that of the IRPS. Figure 5*b* shows a sky map as seen in the IRPS 2.3 μm band. At this wavelength the most striking features are the Galactic plane, the bright Galactic center, and the variable star R Doradus (R.A. = 4^h37^m, decl. = $-62°$). When the DIRBE 2.2 μm sky map is smoothed to IRPS resolution, the Galactic center has a peak intensity of 512 μJy arcsec^{-2}. The absolute calibration factor for the DIRBE 2.2 μm observations has an uncertainty of 3% (W. Reach 1998, private communication). Calibrating the IRPS 2.3 μm intensity against DIRBE 2.2 μm for measurements of the Galactic center (see, e.g., Fig. 4) agreed to within 5% with determinations made using a blackbody source at 0° C. For the J and H bands this provided the only means of calibrating the data as the flux from the blackbody was negligible at these wavelengths, although the low signal-to-noise ratio (S/N) results in an uncertainty of 30%–40% in the result. The calibration assumed the J- and H-band fluxes toward the Galactic center were 289 and 383 μJy arcsec^{-2}, respectively, averaged through the IRPS 3°.8 beam.

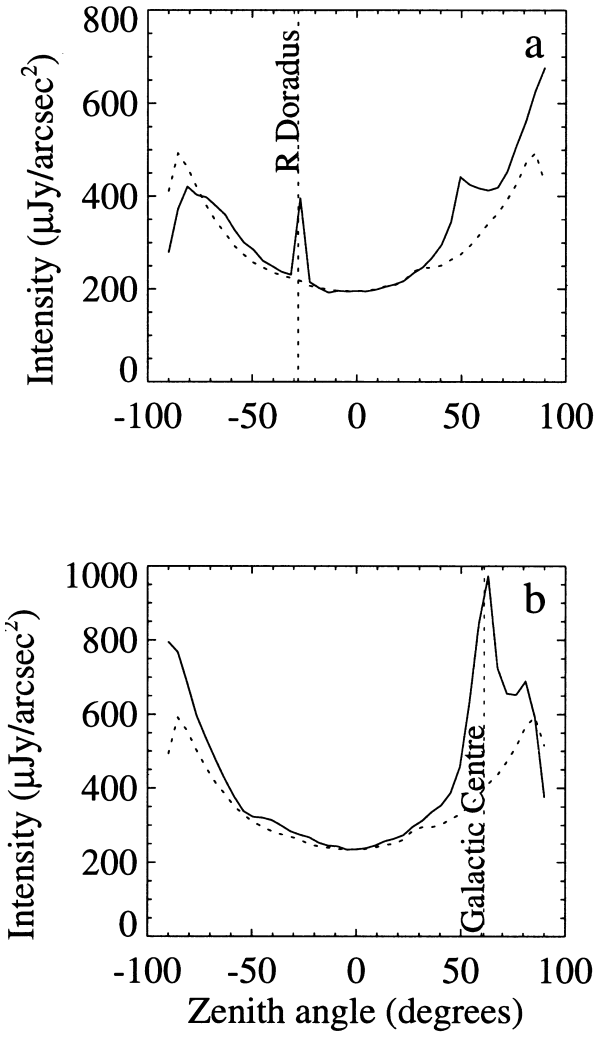

FIG. 4.—K_{dark} (2.3 μm) filter skydip passing through (*a*) R Doradus (4^h37^m, $-62°$) and the plane of the Galaxy (at 16^h37^m, from declination $-25°$ to $-45°$) and (*b*) the Galactic center (17^h45^m). The broken line shows the median dark-sky skydip, normalized to the same zenith intensity.

The K_{dark} map of the southern sky (Fig. 5*b*) was formed by averaging the entire IRPS 2.3 μm data set selected, as much as is possible, for cloud-free conditions. However, the data coverage in right ascension is not uniform, and some residual effects from clouds remain (e.g., the occasional vertically stretched contour). Figure 5*b* is presented to illustrate that the plane of the Galaxy is clearly visible in K_{dark}. For precise comparison between DIRBE and IRPS measurements, an analysis of selected skydips is required.

At the K band the brightest object in the southern sky is the Galactic center, followed by five stars (with $m_K \leq -3$): α Scorpius ($m_K = -3.9$), R Doradus ($m_K = -3.8$), γ Crucis ($m_K = -3.2$), β Grus ($m_K = -3.2$), and W Hydra ($m_K = -3.0$). All of these stars are seen in Figure 5. It is notable how at K_{dark} the Galactic Plane is apparent without the need to subtract a sky background even when observed with a 3 mm diameter telescope! In this respect the IRPS is seeing the Milky Way in K_{dark} in much the same way as our eyes see it in the optical. Only from the Antarctic plateau are the backgrounds so low that the Milky Way can be seen directly in the infrared.

3. SKYDIP ANALYSIS

The atmospheric emission observed originates primarily from airglow emission, OH radicals ~90 km above the Earth modified by the atmospheric transmission, and thermal emission within the atmosphere. These contributors provide different signatures to the skydip profiles, and in this section we discuss how to obtain their magnitudes from an analysis of the skydip shapes.

We solve the radiative transfer equation for the atmospheric emission as a function of wavelength. We suppose that the measured fluxes have contributions from airglow emission, originating above the atmosphere, and from thermal emission within the atmosphere. Absorption within the atmosphere is assumed to occur uniformly and to be described by a single parameter, the optical depth. We neglect any contributions from scattering into the beam. Then the measured flux, $F(\lambda, \theta)$, from a plane parallel atmosphere at a particular wavelength λ and zenith angle θ, is

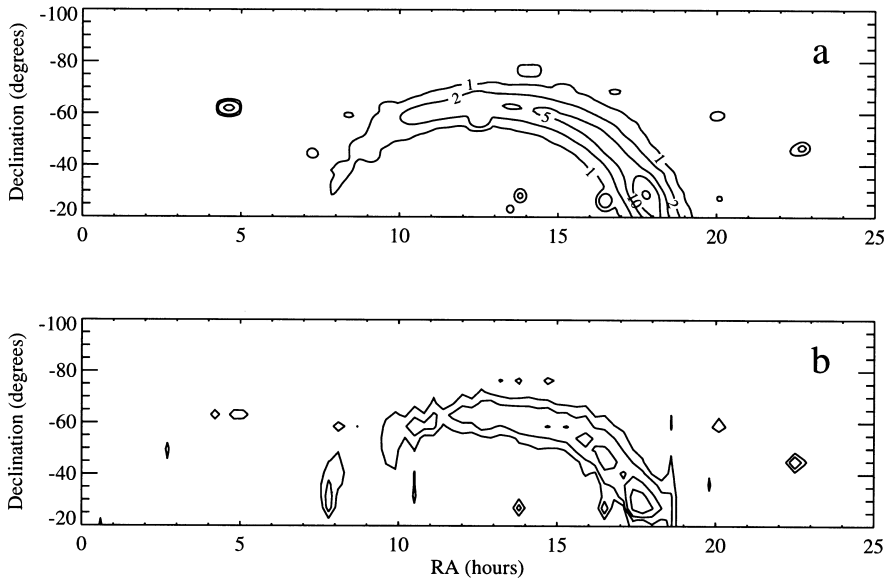

FIG. 5.—(*a*) Contours of DIRBE 2.2 μm intensity in the south celestial sphere, smoothed to the resolution of the IRPS, in MJy sr^{-1}. (*b*) Contours of the $K_{\rm dark}$ sky intensity (in arbitrary units) in the south celestial sphere, as measured by the IRPS using an effective 3 mm diameter aperture telescope. In both cases the Galactic plane is clearly seen with the Galactic center at ($17^{\rm h}45^{\rm m}$, $-29°$). Also seen are the stars α Sco ($16^{\rm h}29^{\rm m}$, $-26°$, $m_K = -3.9$), R Dor ($4^{\rm h}37^{\rm m}$, $-62°$, $m_K = -3.8$), γ Cru ($12^{\rm h}31^{\rm m}$, $-57°$, $m_K = -3.2$), R Hya ($13^{\rm h}30^{\rm m}$, $-23°$, $m_K = -2.5$), W Hya ($13^{\rm h}49^{\rm m}$, $-28°$, $m_K = -3.0$), β Gru ($22^{\rm h}43^{\rm m}$, $-47°$, $m_K = -3.2$), and π Gru ($22^{\rm h}22^{\rm m}$, $-46°$, $m_K = -2.0$).

given by

$$F(\lambda, \theta) = A(\lambda) + F_{\rm OH}(\lambda) \sec \theta e^{-\tau \sec \theta} + B(\lambda, T) \times (1 - e^{-\tau \sec \theta}) , \quad (1)$$

where $F_{\rm OH}(\lambda)$ is the zenith airglow flux, in the absence of any absorption, $B(\lambda, T)$ is the blackbody flux at the effective temperature of atmosphere where thermal emission primarily occurs, and $A(\lambda)$ is a constant offset, corresponding to thermal emission from the instrument, and any other DC component in the signal. $\tau(\lambda)$ is the optical depth of the atmosphere viewed through the zenith.

In the broadband passes used (including the 1% CVF) the transmission (and hence the optical depth) will not be uniform, and in particular some parts may be optically thick while other parts will be optically thin. The former will contribute mostly to the thermal emission, whereas the latter mostly to the airglow emission and also any astronomical source being observed. We approximate this varying transmission by assuming that a fraction of the bandpass, f, is optically thin (i.e., $\tau < 1$), while the rest, $1 - f$, is optically thick (i.e., $\tau > 1$). Then the observed flux becomes

$$F = A + fF_{\rm OH} \sec \theta e^{-\tau \sec \theta} + (1 - f)B(T) + fB(T) \times (1 - e^{-\tau \sec \theta}) . \quad (2)$$

Fortunately this equation can be simplified, depending on whether airglow dominates ($\lambda < 2.3$ μm) or thermal emission dominates ($\lambda > 2.9$ μm). In the former case we obtain

$$F = A + fF_{\rm OH} \sec \theta e^{-\tau \sec \theta} , \quad (3)$$

and, by minimizing the value of chi-squared through fits to the skydips, we can obtain values for A, $fF_{\rm OH}$, and τ for each filter. Figure 6*a* shows the form these curves take as τ is varied, after removing the additive constant and scaling the zenith intensity to unity. For zero optical depth the intensity varies simply as sec θ. For small optical depths it increases with zenith angle, as the increased path length (sec θ) dominates over the extra absorption. However as the optical depth rises the intensity then turns over and starts to drop at larger zenith angle, as the exponential absorption term takes over.

When thermal emission dominates, on the other hand, we obtain

$$F = A + (1 - f)B(T) + fB(T)(1 - e^{-\tau \sec \theta}) . \quad (4)$$

Fitting to the skydips then yields values for f, $B(T)$, and τ as well as the DC term. By assuming the DC term is either all instrumental or all optically thick atmospheric emission, we can derive lower and upper limits to the atmospheric flux, respectively. Figure 6*b* shows the form of these skydips as τ is varied, with the DC component removed and the zenith intensity scaled to unity. For small τ the curves closely follow sec θ and are similar to those for airglow emission (Fig. 6*a*). However, as τ increases, the curves simply flatten out and do not turn over. The limit of large optical depth is uniform emission at all zenith angles; this would correspond to thick fog. We also note that if $\tau \ll 1$, equation (4) becomes

$$F = A + (1 - f)B(T) + fB(T)\tau \sec \theta . \quad (5)$$

Determination of the parameters f, $B(T)$, and τ then becomes degenerate.

Since airglow dominates the emission for the J, H, and K bands, and atmospheric thermal emission dominates at M, it is clear that equation (3) should be applied to the former and equation (4) to the latter. In $K_{\rm dark}$ and 2.43 μm, where we cannot categorically make this statement, we examined how both functions fitted the data. For thermal emission our fits are biased toward fitting the optically thickest parts of a window rather than the clearest parts of it. The background is dominated by wavelengths where τ is greatest, whereas the flux collected from an astronomical source is greatest where the transmission is best (or τ least). Thus we

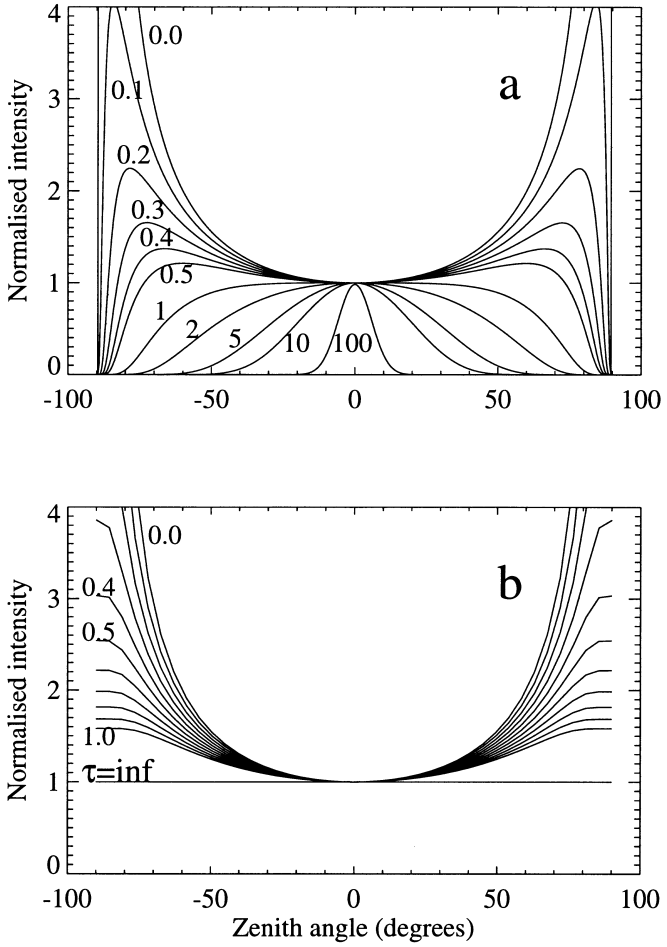

FIG. 6.—Model skydip curves for the zenith intensity, with DC component removed and normalized to unity, for a range of optical depths, τ. (*a*) The upper figure is for a source above the atmosphere, such as airglow, extinguished by the atmosphere. Optical depths are labeled from $\tau = 0$ to 100. (*b*) The lower figure is the case where the atmosphere itself emits radiation. Optical depths vary from 0 to 1 in steps of 0.1, with 0, 0.4, 0.5, and 1.0 labeled.

caution that the parameter τ derived does not fully characterize the atmosphere as regards its performance for astronomical observations, which will be better than this figure of merit.

The CVF spectra obtained at zenith and $z = 76°.5$ also allow estimates of these parameters to be made. However some further assumptions are needed as there is insufficient data to fit a skydip in order to determine them uniquely. For the H band, we can ignore the additive constant and use the ratio of fluxes at $z = 0°$ and $z = 76°.5$ to determine τ directly (from eq. [3]) as a function of wavelength. However, when thermal emission is significant, the DC term cannot be neglected.

4. INTERFERENCE

Our data were obtained remotely, through a variety of observing conditions. In order to assess the quality of the site we need to determine not only what the sky fluxes are during the best observing periods but also how often those periods occur and what sources of interference there are. As we discuss below, the meteorological data obtained by a (human) observer at the Pole are not reliable for this purpose. We had to resort to analyzing the shapes and absolute fluxes of the skydip profiles to determine the suitable data for further analysis. There are three principal sources of interference: clouds, twilight, and moonlight. In addition auroral emission might conceivably contribute to the flux in the infrared windows. We discuss the first three here and auroral emission in § 5.5.

4.1. *Clouds*

The effects of clouds on these measurements have been considered at length, especially in comparison with human visual meteorological observations. The measurement of clouds during a moonless Antarctic night presents obvious difficulty, and there have been several studies to assess the accuracy of human visual measurement during these conditions. Studies by Schneider, Paluzzi, & Oliver (1989) and Hahn, Warren, & London (1985) show a significant underestimation of thin and scattered cloud by human observers during dark moonless conditions, whereas visual measurements of opaque cloud are less affected by background sky illumination. In particular, they show that estimates of reported cloud are significantly related to lunar illumination. The IRPS data were compared with the trihourly meteorological cloud observations for DOY 147–235 (obtained as part of the standard meteorological record for the site). Comparison of the $K_{\rm dark}$ (2.3 μm) filter zenith intensity with the cloud estimates showed poor correlation. However, the IRPS also recorded ambient temperatures and these followed the meteorological data, indicating that the two data sets were collected simultaneously. We thus had to revert to examining our data to determine when it was affected by clouds rather than using the meteorological records.

The presence of thick clouds is clearly detectable in a skydip profile, as it departs significantly from a secant curve, particularly at low elevations. Periods of heavy opaque clouds produced a flattened or misshapen skydip curve. High correlation was obtained between "good" skydips (i.e., closely approximating a secant curve) and low zenith intensity. That is, the presence of clouds leads to both increased zenith intensity and an asymmetric skydip curve.

Cloud effects are demonstrated in Figures 7*a*, 7*b*, and 7*c*, where the zenith fluxes at H, $K_{\rm dark}$, and M are plotted against the solar zenith angle. Alternating periods of cloudiness and clear sky cause periodic rising and falling of zenith intensity when the Sun is more than 10° below the horizon. When less than 10°, scattered sunlight also contributes, as we discuss in the next section. This figure also shows that in the $K_{\rm dark}$ band viewing conditions at the Pole are regularly very dark indeed.

4.2. *Sun (Twilight)*

The zenith intensity measurements in the H and $K_{\rm dark}$ band (Figs. 7*a* and 7*b*) show a clear and sudden increase in sky brightness at a solar zenith angle $z = 100°$. Figure 8, which shows the height of the terminator as a function of solar angle, shows that this corresponds with the first illumination of the atmosphere at around 100 km, and perhaps a little lower if refraction is considered. This effect has a strong wavelength dependence. For every set of skydip measurements, a spectrum was also obtained in the H–K band, 1.4–2.5 μm. For solar zenith angles greater than 101° the spectra are quite constant. Figure 9 shows a sample of spectra between 1.4 and 2.0 μm that have been normalized by division of the wintertime dark sky spectrum. At

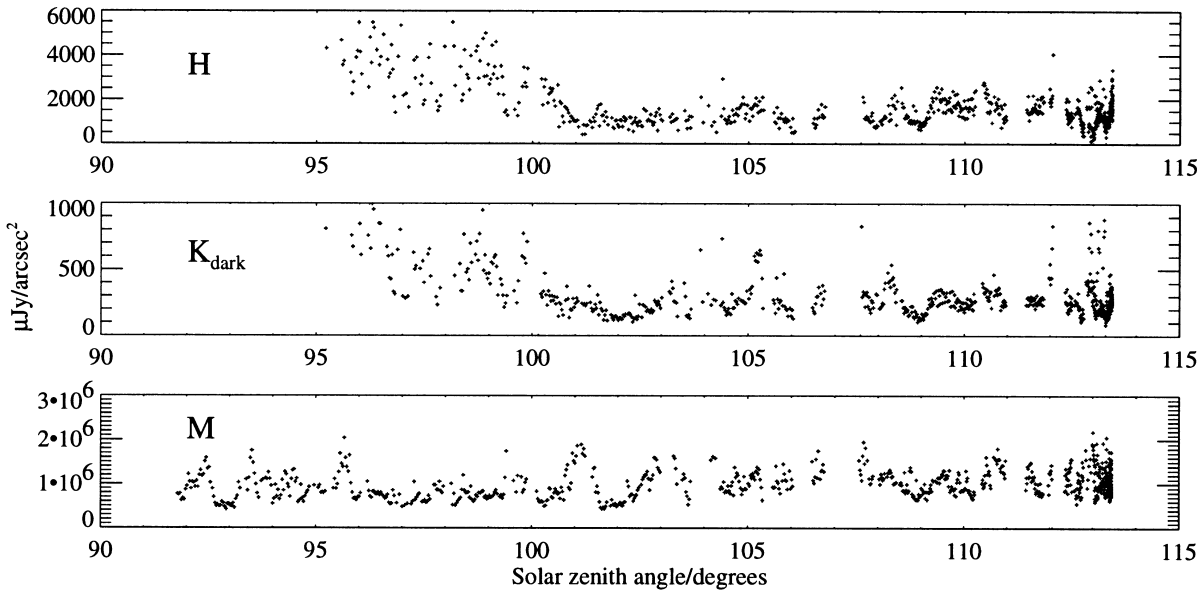

FIG. 7.—Zenith intensity in μJy arcsec^{-2} in the H, K_{dark} (2.3 μm), and M bands vs. solar zenith angle at the South Pole, winter 1995

$z = 100°$ the spectrum is essentially flat and typical of the wintertime. However, by $z = 98°$ (corresponding to the illumination of atmosphere at 60 km and above), there is a significant increase in intensity across the whole band. At $z = 97°$ the upper stratosphere is illuminated. A trend to higher intensity at shorter wavelength is also apparent. At $z = 92°$ the troposphere is illuminated and the general shape of the spectrum follows a λ^{-4} law, suggesting that the observed light in this band is probably from Rayleigh scattering from the stratosphere and troposphere. It is unlikely to be from enhanced airglow, because wavelengths of peak intensity in Figure 9 ($z = 92°$) are anticorrelated with the intensity peaks in the dark sky spectrum. The airglow component must remain roughly constant as the scattered component rises dramatically.

4.3. *Moon*

Moonlight scattered from clouds was detected by the IRPS. The effect is evident when J-band zenith intensity measurements are sorted according to an approximate index of lunar brightness, in our case the lunar elevation angle multiplied by fractional disk illumination. During times of lunar illumination, J-band zenith intensity measurements are more scattered and significantly brighter. In Figure 10 we plot J-band versus K-band sky flux when the Moon is up and when it is down. It is clear that there is an increase in the relative J-band intensity when the Moon is up. The effect may also exist to a lesser degree in the K_{dark} band, but it is completely absent in H, K, and M-band observations. We suggest that moonlight scattered from clouds is being observed, the shorter wavelength of the J band (1.25 μm) being most susceptible to scattering, the effect also being detectable at K_{dark} as the sky emission there is so weak.

4.4. *Fraction of Dark Sky Data*

The data presented in this paper were collected during the winter of 1995. Between DOY 147–261, 881 2 hr observing sequences were made, representing 64% of the potential observing time during that period. However, not all of the data were suitable for further analysis. For example, as described in § 4.2, it was discovered that the infrared sky became truly dark only with $z > 100°$, while the instrument was run until $z = 92°$. It was also impossible to remove the effect of cloud completely, but some obvious effects were noted and the data excluded from subsequent analysis. Clouds are most easily detected by increased zenith intensity and asymmetry in the skydip curves, especially in the K_{dark} band. Occasionally electronic or software failure would also generate records with zero values or impossibly

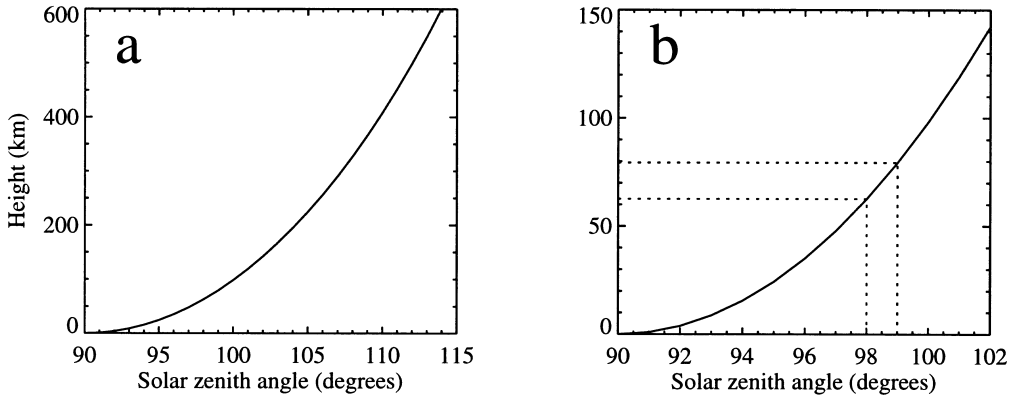

FIG. 8.—Height of the day/night terminator during twilight (not allowing for atmospheric refraction or scatter)

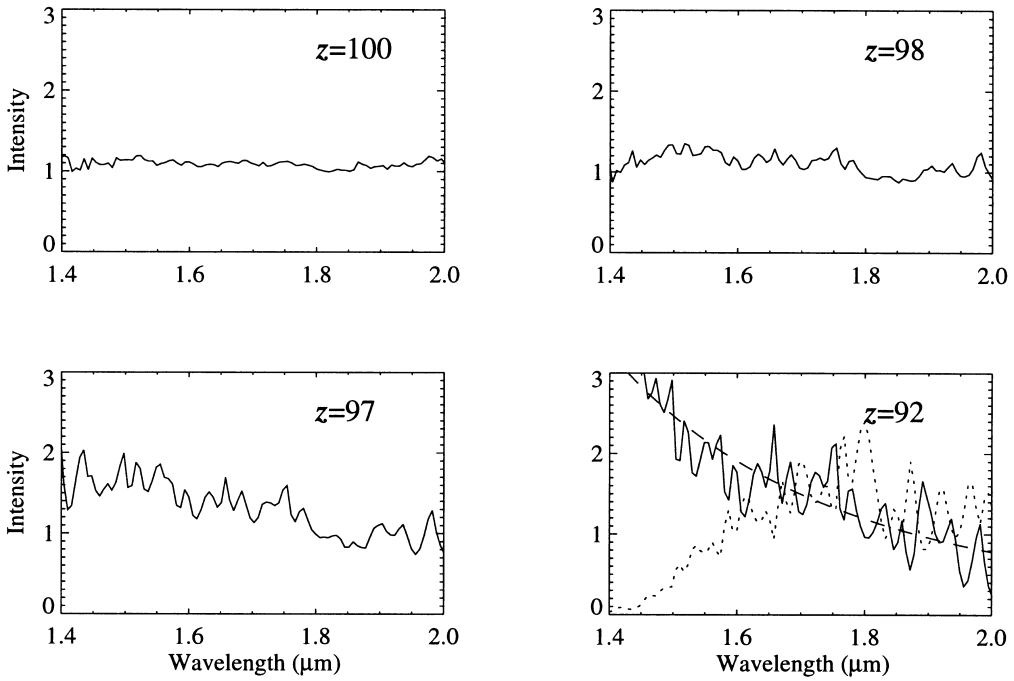

FIG. 9.—Normalized H-band spectra during twilight conditions, at the South Pole in 1995, for solar zenith angle z varying from 100° to 92°. The spectra have been divided by the median dark-sky spectrum. The curve for $z = 92°$ also has a λ^{-4} Rayleigh curve overlaid (*long-dashed line*), as well as the median (unnormalized) dark-sky spectrum (*short-dashed line*).

large transients in the skydip curves. Such data were rejected. Finally, there were times when the IRPS detector warmed above its nominal operating temperature of 65 K, resulting in increased output. We employed the following criteria to select dark sky data. Firstly data were considered only when the detector temperature was <75 K. They were then selected for solar $z > 100°$. Selecting cloud-free data based on skydip asymmetry required care as bright stars, and especially regions near the Galactic center, can cause large asymmetry in the skydip curves. To test for clouds, the $K_{\rm dark}$ skydip curves were normalized to a zenith intensity of unity and one side of the skydip curve subtracted from the other, for $|z| < 72.^{\circ}5$. Data were rejected if the difference was too large. In all, 55% of the total data were deemed suitable for further analysis. This is 87% of the data when the instrument was working well and with $z > 100°$. Table 2 summarizes the statistics. The data that passed these cloud-free criteria we refer to as the dark-sky data. They could also be further sorted according to the zenith intensity figure. Such sorting showed that skydips with generally lower zenith intensities more closely resembled a sec z curve, suggesting that even the carefully selected dark-sky skydips still contained residual effects from cloud and fog. While it is not readily quantified how much data this applies to, examination of the histograms of the sky flux distributions suggests that possibly one-half the remaining data may be affected in some way by the presence of cloud. The effect of moonlight illuminating cloud was readily detected only at the J band, and data collected during times when the moon was up accounted for only a few percent of the total. In general, data collected during times of lunar illumination were not removed from our analysis.

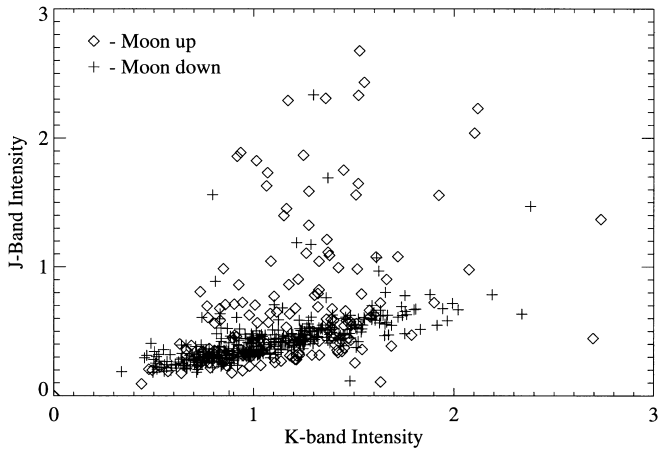

FIG. 10.—Simultaneous measurements of J- and K-band zenith intensity, during times of darkness (*crosses*) and lunar illumination (*diamonds*). Increased J-band intensity is evident when the Moon is up.

5. RESULTS

5.1. *Zenith Intensity*

Figure 11 shows histograms of the zenith sky brightness intensity from the six filters through which sky dips were made (J, H, K, $K_{\rm dark}$, M, and 2.43 μm CVF) and three wavelengths on the L-band CVF (3.1, 3.6 and 4.0 μm). These histograms were produced from data that do not show any obvious interference as described in the previous section, but it is important to note that these distributions include unresolved interference by cloud, which generally biases them toward higher intensity. For the M-band, and probably the L-band CVF data, this includes a significant DC instrumental component, which we discuss further in § 5.3. Table 3 lists the typical zenith intensities for the peaks of these distributions and compares them with typical results for temperate sites (see also § 6). These fluxes, in μJy arcsec^{-2}, range from 300 to 600 for J, from 800 to 2000 for H, from 300 to 700 for K, from 150 to 300 for $K_{\rm dark}$, and from 80 to 200 in the lowest part of the $K_{\rm dark}$ window at 2.43

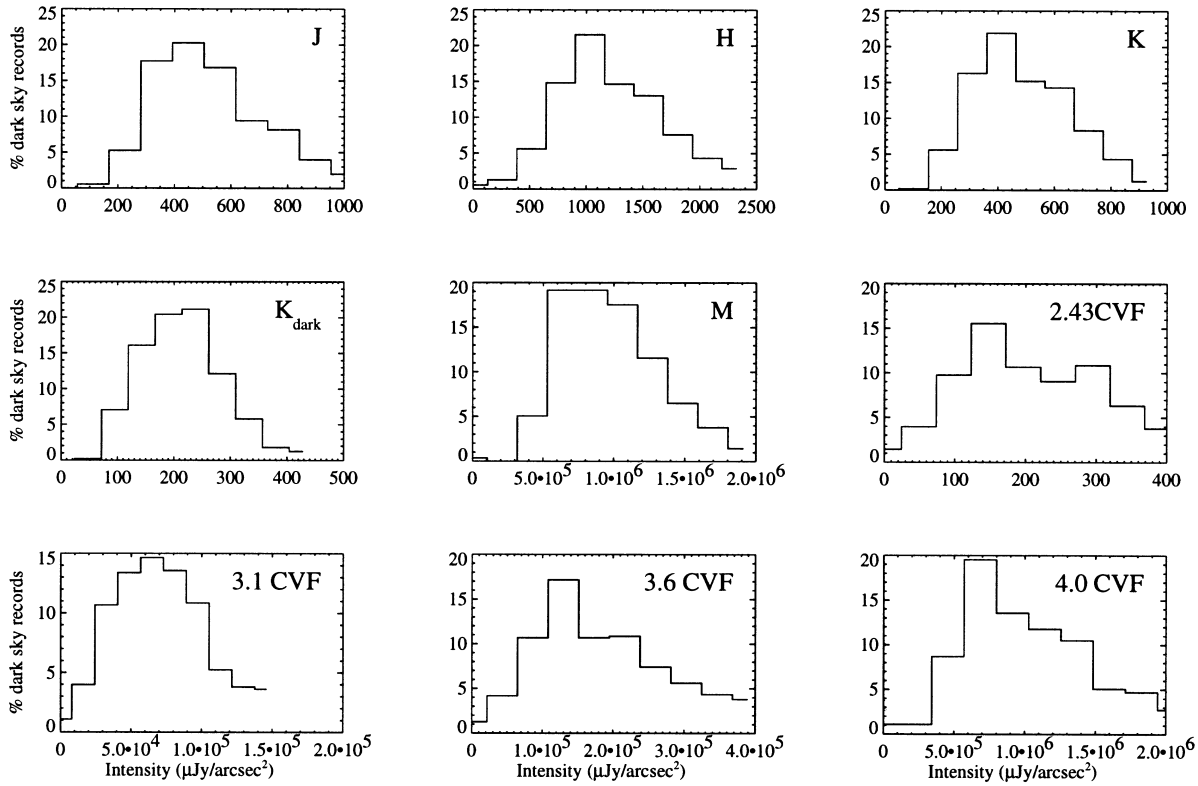

FIG. 11.—Histograms of zenith intensity measured during wintertime at the South Pole in 1995, through the broadband J (1.25 μm), H (1.65 μm), K (2.2 μm), K_{dark} (2.3 μm), and M (4.8 μm) filters, and a 1% CVF filter at 2.43, 3.1, 3.6, and 4.0 μm. For the L- and M-band fluxes the signal contains a significant instrumental component (see text). Zenith intensities in units of μJy arcsec^{-2} are plotted against the fraction of dark-sky data in the flux bin.

μm. In the L band, typical fluxes are 90–300 mJy arcsec^{-2}, and in the M band 0.7–1.5 Jy arcsec^{-2}, including the DC component.

5.2. *Contributions to the Emission*

The sky fluxes recorded by the IRPS have several contributors to them, principally airglow, scattered solar and lunar radiation, and thermal emission. As discussed in § 4.2, scattered sunlight is evident when the Sun is less than 10° below the horizon and is most prominent at shorter wavelengths because of its Rayleigh nature. Airglow emission arises primarily from the vibration-rotation lines of OH, from altitudes 80–90 km above the surface. The primary band peaks in intensity near 3 μm, and the first broad overtone band lies between 1.5 and 2.2 μm. Between 2.27 and 2.45 μm the airglow flux is minimum. Since nighttime OH airglow primarily results from the molecular recombination of daytime photochemical products, mid-latitude airglow

TABLE 3

COMPARISON OF ZENITH SKY FLUX INTENSITIES BETWEEN SITES

	INTENSITY				
BAND/WAVELENGTH	Siding Spring (μJy arcsec^{-2})	Mauna Kea (μJy arcsec^{-2})	South Pole (μJy arcsec^{-2})	South Pole (mag arcsec^{-2})	$-60°$, 5% Emission (μJy arcsec^{-2})
J (1.25 μm)	1000–1500	~900	300–600	16.8–16.0	8×10^{-11}
H (1.65 μm).....	1500–3000	~2500	800–2000	15.2–14.2	2×10^{-5}
K (2.2 μm)	6000–15,000	...	300–700	15.8–14.9	5×10^{-2}
K_n (2.1 μm)	3000–7000	~3000	~400	15.6	2×10^{-1}
K_{dark} (2.3 μm)	~4000	...	150–300	16.4–15.7	7×10^{-1}
2.43 μm	~20000	...	80–200	17.0–16.0	3
3.10 μm	$\sim 1 \times 10^6$	...	$0.3–1 \times 10^5$	9.6–8.9	5×10^2
3.60 μm	$1–8 \times 10^6$	$\sim 3 \times 10^6$	$0.9–3 \times 10^5$	8.5–7.3	7×10^3
4.00 μm	$5–20 \times 10^6$	...	$0.5–1.5 \times 10^6$	6.6–5.4	3×10^4
M (4.8 μm).....	$\sim 100 \times 10^6$	$\sim 80 \times 10^6$	$0.7–1.5 \times 10^6$	5.7–5.0	3×10^5

NOTE.—Zenith intensities for different wavebands, as measured at the Siding Spring (Australia), Mauna Kea, and South Pole observatories. Fluxes are given in μJy arcsec^{-2}, and for South Pole also in mag arcsec^{-2}. For 3.1 μm and longer wavelengths the figures provide upper limits, on the assumption that the DC component is all atmospheric emission. Siding Spring values are a compendium obtained with a variety of instruments, including the IRPS, on the AAT and the Australian National University 2.3 m telescope. Mauna Kea values are taken from the manual for the NSFCAM instrument on the IRTF. The final column gives, for comparison, the flux from a graybody at $-60°$ C (the average wintertime temperature) and 5% emissivity.

fluxes vary diurnally. At the Pole the airglow layer will be shielded from sunlight for 4 months a year, providing us with an opportunity to study the effect of absence of sunlight on the total flux.

Finally, there is thermal emission from the atmosphere. Its intensity is effectively the blackbody flux at the temperature of the dominant emitting layer, times the emissivity of the layer. Thermal emission dominates at temperate sites longward of 2.2 μm. At the Pole it remains minimal until 2.5 μm. Wavelength regions of high transmission have low emission, and opaque regions the highest. Furthermore, the stability of the background level depends primarily on the fluctuations in the emissivity of a particular window, rather than fluctuations in the temperature.

5.3. *Profile Fitting*

As discussed earlier, the skydip data were examined to remove any profiles affected by cloud, Moon, or twilight emission. Of this dark-sky data the median skydip profile for the darkest 20% of the data was then selected. We refer to these as the darkest-sky data. Chi-squared minimization of equation (3) (for airglow) or equation (4) (for thermal) was applied to these profiles, to yield the various parameters that quantify the emission of the atmosphere at a given wavelength. Skydip intensity measurements are made at elevation increments of 4°.5, which provided a 35 point curve from which the chi-squared minimization could be determined (i.e., angles $z = \pm 76°.5$ on either side of zenith). As also discussed in § 3, while it is clear that equation (3) (airglow) applies to the J- and H-band data and equation (4) (thermal) to the M-band data, it is not immediately obvious which is applicable for the K, $K_{\rm dark}$ (2.3 μm) and 2.43 μm CVF data, so both fits were applied. Table 4 presents the parameters derived from these fits, which are shown in Figure 12. These have been normalized so that the zenith flux is unity. The calibration factor relates this to the zenith intensity in μJy arcsec^{-2} for the darkest 20% of the dark-sky data. The median intensity for all the dark-sky data is also listed and is typically twice as high as the darkest-sky value.

As can be seen from the table, the J- and H-band data are well matched by the airglow fit (eq. [3]), with a negligible DC component, and with $\tau = 0.13$. The darkest sky zenith fluxes at the South Pole are ~ 320 μJy arcsec^{-2} at J (1.25 μm) and ~ 610 μJy arcsec^{-2} at H (1.65 μm), with median values typically about twice this level. The M-band data is also well matched by the thermal fit (eq. [4]), but this time with a significant DC component containing 90% of the zenith signal, and with $\tau = 0.3$. The DC component almost certainly has a significant instrumental contribution (a 5% emissive mirror at $-55°$ C will contribute 0.5 Jy arcsec^{-2}).

However we cannot quantify from our data its precise contribution and therefore what fraction of the DC component arises from optically thick atmospheric emission. If the DC component were all instrumental, then the median zenith intensity would be 0.08 Jy arcsec^{-2}, whereas if it were all atmospheric the zenith intensity would be 0.8 Jy arcsec^{-2}, with median values 70% higher. In practice, it is likely that about one-half the emission is atmospheric, if the estimate above for the mirror emission is reasonable. While the parameter τ may seem high, it must be remembered that its magnitude is biased toward the most emissive parts of the window. The optically thin parts of the M-band window will contribute little to the sky flux but most to the flux measured from an astronomical source.

It remains to explain the sky flux in the K, $K_{\rm dark}$, and 2.43 μm filters. Even for a 10% emissive atmosphere at $-40°$ C (the highest temperatures reached in the inversion layer), the flux is only 45 μJy arcsec^{-2}, approximately one-half the lowest fluxes measured. For K and $K_{\rm dark}$ both the thermal and airglow fits give small values for the DC offset. However, the thermal fit also yields $\tau = 0.32$ for both bands, which seems unreasonably large given that any optically thick DC component must be small. In addition, the skydips and the parameters derived from them are similar both in form and in magnitude to those derived for J and H, which are dominated by airglow emission. It seems reasonable to conclude that in both the K and 2.3 μm filter bands residual airglow, rather than atmospheric thermal emission, is the major contributor to the emission (in the next section we also discuss why auroral emission probably does not contribute). This also explains why the sky background in the $K_{\rm dark}$ band is not as low as was first speculated (Harper 1988). Furthermore, the ratio of the CVF spectra (see § 5.4) of sky flux at 76°.5 to that at the zenith (Fig. 13) is 3.0, from 1.5 to 1.8 μm and 2.1 to 2.2 μm, and then falls, reaching 1.8 by 2.4 μm. A ratio of 3.0 is thus a characteristic value for airglow emission in clean atmospheric windows, and 1.8 is

TABLE 4

PARAMETER FITS TO SKYDIPS

Waveband	Fit	A	B	τ	Darkest Sky (μJy arcsec^{-2})	Dark Sky (μJy arcsec^{-2})
J	Airglow	0.05 ± 0.05	1.1 ± 0.1	0.13 ± 0.01	320	540
H	Airglow	0.01 ± 0.05	1.15 ± 0.05	0.13 ± 0.01	610	1300
K	Airglow	0.2 ± 0.1	0.95 ± 0.05	0.13 ± 0.01	280	520
K	Thermal	0.13 ± 0.1	3.2 ± 0.1	0.32 ± 0.02	280	520
$K_{\rm dark}$	Airglow	0.1 ± 0.1	1.07 ± 0.08	0.13 ± 0.01	130	240
$K_{\rm dark}$	Thermal	0.04 ± 0.08	3.6 ± 0.2	0.32 ± 0.04	130	240
2.43 μm.....	Airglow	0.3 ± 0.2	0.8 ± 0.2	0.14 ± 0.03	70	180
2.43 μm.....	Thermal	0.2 ± 0.15	2.5 ± 0.3	0.4 ± 0.1	70	180
M	Thermal	0.90 ± 0.01	0.35 ± 0.01	0.32 ± 0.01	8.0×10^5	1.3×10^6

Results from parameter fitting to skydips, applying $A + B \sec \theta e^{-\tau \sec \theta}$ to airglow bands and $A + B(1 - e^{-\tau \sec \theta})$ to thermal bands. These fits were made to the median of the darkest-sky data. For K, $K_{\rm dark}$ (2.3 μm) and 2.43 μm results from both types of fit are shown. The zenith intensities, equivalent to a scaling factor for A and B, and equal to $A + Be^{-\tau}$ and $A + B(1 - e^{-\tau})$, respectively, are also given in the darkest sky column. The dark sky column gives the median intensity of all the skydips that passed the selection criteria for acceptance, rather than just the darkest 20% of them.

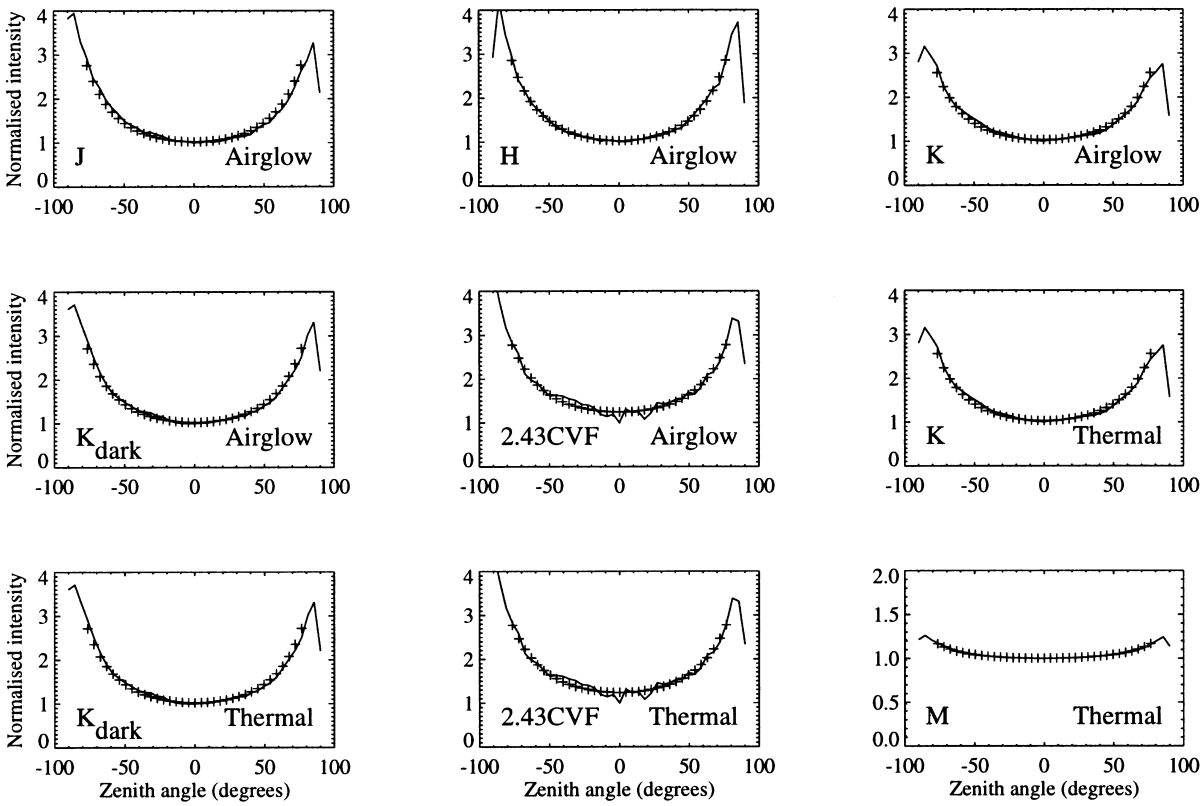

FIG. 12.—Fits (*crosses*) to the median of darkest 20% of the dark-sky skydips, for data with zenith distance $\leq 76.^{\circ}5$, applying the airglow-emission fit (eq. [3]) to the J, H, K, K_{dark} (2.3 μm), and 2.43 μm CVF data and the thermal-emission fit (eq. [4]) to the K-, K_{dark}-, 2.43 μm CVF–, and M-band data. All fits have been normalized to a zenith intensity of unity and can be directly compared to the theoretical curves in Fig. 6. Parameters derived from these fits are listed in Table 4.

presumably characteristic when thermal emission dominates. This would suggest that airglow emission contributes until 2.4 μm, and in particular airglow from the short-wavelength part of the K_{dark} window (i.e., 2.2–2.3 μm) dominates the emission in the band. The darkest zenith fluxes are ~ 130 μJy arcsec^{-2} in the 2.3 μm filter and ~ 280 μJy arcsec^{-2} in the K band. Median values are $\sim 80\%$ higher than this.

Caution needs to be applied to overinterpreting the 2.43 μm CVF sky dips as the S/N is poor, but the thermal fits yield a significant DC component, $\sim 20\%$ of the zenith signal. This can have contributions from both the instrument and any optically thick atmospheric emission in the bandpass. Applying the airglow fit to the same data also yields a DC component, $\sim 30\%$ of the zenith signal. However there is no reasonable interpretation for such a large signal in this model. Thus we conclude that at 2.43 μm we are indeed measuring emission from within the atmosphere, but the precise contribution of the instrumental component to the signal cannot be assessed. The rather high value of τ derived is probably an artifact from fitting the DC component of the signal. With our stare mode of operation, we are at the limit of sensitivity of the instrument for such small fluxes, and a chopped measurement is necessary to quantify the sky level further. The 2.43 μm zenith sky flux is as low as 70 μJy arcsec^{-2}, and perhaps as much as 20% of this is from our instrument. Median values are typically twice as large.

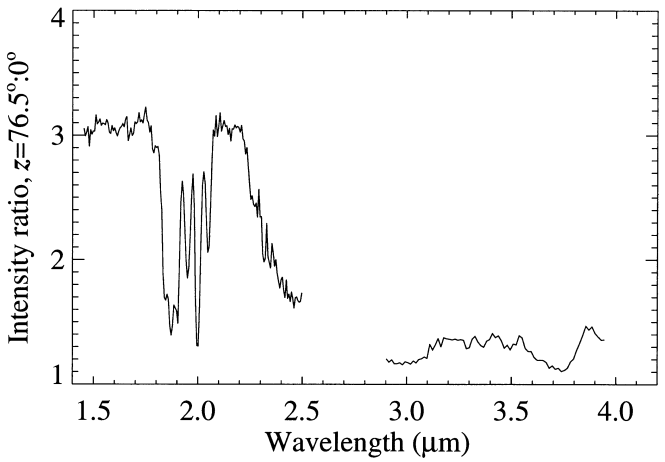

FIG. 13.—Intensity ratios of the median dark sky spectra obtained with the HK- and L-band CVFs, for the fluxes at $z = 76.^{\circ}5$ to those overhead. Table 5 summarizes the results.

5.4. *Spectral Flux Ratios*

In Figure 13 we present the intensity ratio of the median dark-sky spectrum obtained at $z = 76.^{\circ}5$ to that at the zenith, for both the HK- and L-band CVFs. Table 5 summarizes the data ("median" here refers to the complete spectrum, not to individual data points). Purely optically thin emission from a plane-parallel atmosphere would produce a ratio of 4.3, which is clearly not approached. However the validity of such a model at high zenith angle is questionable, and it is more instructive to consider how the measured ratio changes with wavelength. The H-band window from 1.5 to 1.8 μm, and the K band from 2.1 to 2.2 μm, which are both clean and where only airglow contrib-

TABLE 5

SKY FLUX RATIOS AT 76°.5 TO ZENITH

Wavelength (μm)	Ratio	Comment
1.25.....	3.0	J band, airglow
1.65.....	3.0	H band, airglow
1.5–1.8	3.0	CVF, clear window, airglow
1.85–1.9	1.3	CVF, poor transmission, airglow
2.1–2.2	3.0	CVF, clear window, airglow
2.2–2.4	3.0 → 1.8	CVF, clear window, transition from airglow to thermal
2.4–2.5	1.8	CVF, clear window, thermal
3.2–3.8	1.3	CVF, clear window, thermal, DC component
M.....	1.2	M band, thermal, DC component

NOTE.—Intensity ratios of sky fluxes at zenith angle 76°.5 to zenith, from the HK and L CVF spectra, and selected broadband ratios derived from the skydips.

utes, produce a ratio of 3.0. At 1.9 μm, in the middle of the absorption feature from H_2O, it falls to 1.3, a value indicating absorption but not complete obscuration. At 2.4 μm, where thermal emission dominates, the ratio has dropped to 1.8, and between 2.2 and 2.4 μm it falls from the airglow value (3.0) to the thermal value (1.8). This fall presumably marks the change from airglow to thermally dominated regimes. Throughout the L band the ratio is $\sim$1.2–1.4, and the skydips at M provide a ratio of 1.2. Since this latter value is strongly affected by a significant DC component, this presumably applies across the L band as well, and to a lesser extent at the long wavelength end of the K band.

5.5. *Infrared Aurora*

Even during times of dark skies (as measured by the IRPS) there is still a significant distribution of zenith intensities in the near-infrared. This may still be the result of unresolved thin uniform cloud, but other sources were considered, in particular infrared auroral contamination.

The geomagnetic latitude of the geographic South Pole is $-74°$, which places it in an aurorally active region. Little is known about possible infrared auroral emission rates in the 2–4 μm wavelength band, but since auroral emission could not be ruled out, the time series of H-, K-, and L-band zenith intensities were cross-correlated with several geophysical parameters. At the Pole during winter, continuous measurements are made of many geophysical parameters, including data from riometer, magnetometer, and photometric instruments. A riometer (or relative ionospheric opacity meter) measures attenuation of $\sim$30–50 MHz cosmic radio noise by the Earth's ionospheric D region. The absorption is caused by increased ionization in lower, denser regions of the ionosphere because of the downward precipitation of charged particles. Times of strong absorption are normally associated with auroral activity, as are times with higher variation in the geomagnetic field and in particular the variation in the horizontal component of the local field. At the Pole during winter continuous measurements are made of the 630 nm (oxygen) and 427.8 nm (N_2^+) auroral emission lines (Wu & Rosenberg 1992), which directly indicate overhead auroral activity. The intensity of the 427.8 nm provides a measure of the total electron energy deposition of an aurora, while the relative intensity I(630 nm)/I(427.8 nm) gives a measure of the height of an aurora. This ratio decreases when higher energy electrons penetrate deeper into the atmosphere. The global geomagnetic activity 3 hr K_p index provides another measure of the likelihood of auroral emissions. Cross correlations between these geophysical data and time series of the H-, K-, and K_{dark}-band zenith intensities failed to reveal any significant correlation. As an example, we show in Figure 14 the 630 nm emission versus the K_{dark} sky emission. We take this lack of correlation as strong evidence that infrared emission from aurorae makes no measurable contribution to the infrared sky brightness.

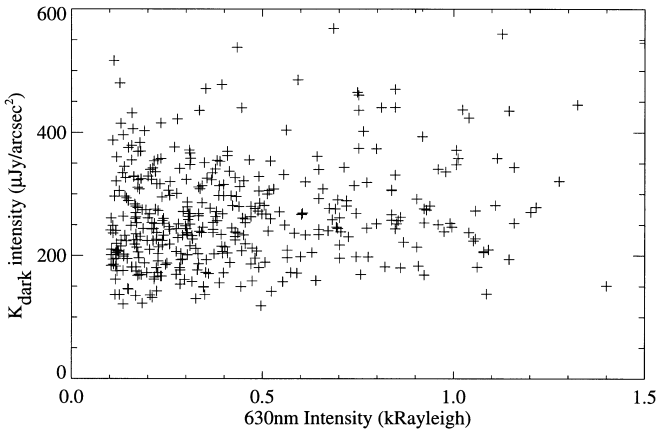

FIG. 14.—630 nm emission (from Wu & Rosenberg 1992) vs. K_{dark} (2.3 μm) sky (zenith) emission. There is no correlation between this measure of auroral activity and the flux from the sky in the K_{dark} band.

A cross check between the measured zenith intensity and numerous IRPS instrumental parameters, such as the temperature of the external mirror, window, detector, and voltages of IRPS electronics, showed no correlations. It therefore seems most probable that the distributions of zenith intensities as shown in Figures 7*a* and 7*b* arise mostly from unresolved cloud effects.

6. COMPARISON WITH OTHER SITES

As discussed by Ashley et al. (1996), the sky flux in the K_{dark} (2.27–2.45 μm) window is typically some 20 times less at the South Pole than the flux in the K_n (2.1 μm) window at temperate sites such as Siding Spring Observatory. Similarly, the flux in the L-band window (3–4 μm) is also some 20 times lower than at Siding Spring. We confirm these results and extend them to the 1–5 μm near-IR region. Figure 15 shows a comparison between spectra of the K- and L-band sky at the Pole and those measured at Siding Spring. We also list in Table 3, with our measured sky fluxes at Pole, typical values measured at Siding Spring and

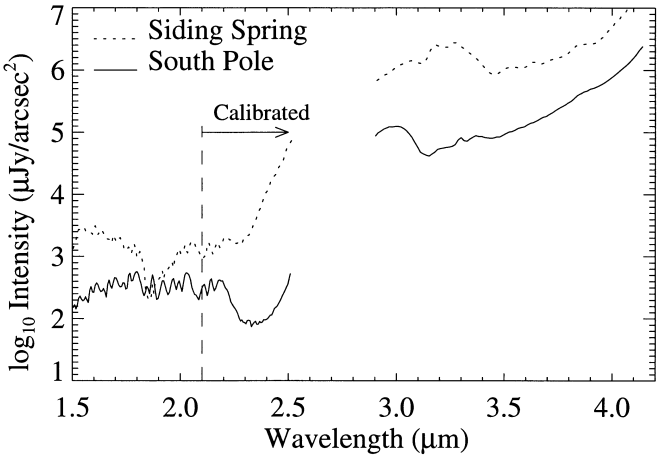

FIG. 15.—Sky emission measured across the H, K and L bands at Siding Spring Observatory in Australia and at the South Pole. A nominal calibration factor has been applied to the data shortward of 2.1 μm.

Mauna Kea (the latter as measured by the NSFCAM on the IRTF). The values for Siding Spring are representative of good observing sites, and will be comparable, for instance, with Kitt Peak in the United States, although, as can be seen from the table, excellent sites such as Mauna Kea provide somewhat lower values.

An interesting comparison of our results for the 2 μm window can be made with those of Mandolesi et al. (1998), who observed the sky emission from a balloon-borne telescope through seven spectral bands from 2 to 4.6 μm with spectral resolution from 20 to 50. Their measurements, obtained at an altitude of 38 km in temperate latitudes with a cryogenic instrument and ambient temperatures of $\sim -80°$ C, are remarkably close to the lowest sky fluxes we measured at the South Pole. At 2.02, 2.15, and 2.28 μm they find backgrounds of 290, 490, and 300 μJy arcsec^{-2}, dropping to $\sim$45 μJy arcsec^{-2} at 2.39 and 2.5 μm. The first three measurements are similar to the lowest fluxes we measure for the airglow, and in particular the 2.28 μm flux is dominated by the airglow. This is consistent with our conclusions based on the skydips through the $K_{\rm dark}$ (2.3 μm) filter. At 2.39 and 2.50 μm the sky fluxes are typically one-half of the lowest levels we record but an order of magnitude greater than expected if it were purely thermal emission from the atmosphere at the ambient temperature. However our thermal skydip fits to the 2.43 μm data on the very best days yield a zenith flux of $\sim$55 μJy arcsec^{-2} (when the DC component is removed, see § 5.3), remarkably close to the balloon measurements at 38 km altitude and $\sim -80°$ C. It would seem that the fluxes measured at the Pole at these wavelengths cannot originate from atmospheric layers close to the ground. Thus they are not emitted from the $\sim$100–200 m thick boundary layer above the Antarctic plateau, which produces the visual seeing (see Marks et al. 1999).

The fluxes obtained by Mandolesi et al. (1998) at 3.54 and 4.61 μm, 0.5 and 10 mJy arcsec^{-2}, are 2 orders of magnitude lower than we measure at Pole but consistent with thermal emission at $-80°$ C from an atmosphere with 2%–3% emissivity, as might be expected from the altitude of the observations.

We find that the flux from the airglow is also less at the Pole than at temperate sites. In the J band (1.25 μm) the sky at Pole is typically only 20%–30% as bright as at Siding Spring, and in the H band (1.65 μm) it is one-half as bright. Our measurements were made in the latter part of the Polar winter, after the airglow layer had been shielded from direct sunlight for at least a month, so we cannot tell whether this reduction applies all winter or is a result of the lack of direct heating from the Sun. Nevertheless it is clear that significant background reductions are encountered from 1 to 2 μm and that any instrument deployed to take advantage of the reduced thermal background beyond 2.2 μm can also usefully be employed down to 1 μm. Also evident from the CVF spectra is that windows in H and K are cleaner, being both broader and more sharply defined at their edges.

Finally we also find significant reductions in the M band (4.8 μm), although we cannot quantify the exact level of the background because of the uncertainty in the amount of instrumental contribution to the flux. However the background is of order 1% of the level at Siding Spring and Mauna Kea. This marks a very significant reduction in a window that so far has received little attention from astronomers because of the great difficulty in conducting observations through it from temperate sites.

7. CONCLUSIONS

We have undertaken extensive measurements of the sky background emission above the South Pole from 1 to 5 μm during winter-time conditions. When conditions are dark (as determined by the selection criteria summarized in Table 2), which occurred for approximately 85% of the time in 1995, we find the following results.

1. Thermal emission dominates beyond 2.4 μm, and airglow emission dominates at shorter wavelengths with, in particular, airglow emission dominating in the short wavelength part of the $K_{\rm dark}$ band (i.e., from 2.27 to $\sim$2.4 μm).

2. Typical thermal sky backgrounds are 80–200 μJy arcsec^{-2} at 2.4 μm, 100–300 mJy arcsec^{-2} at 3.6 μm, and $\sim$0.5 Jy arcsec^{-2} at 4.8 μm. These fluxes are 20–100 times less than at temperate sites such as Siding Spring or Mauna Kea Observatory.

3. The darkest window for observations at the South Pole is from 2.35 to 2.45 μm, where background fluxes may fall to as low as $\sim$50 μJy arcsec^{-2}. It appears that this background is not local and may include residual airglow emission.

4. The L and M bands may, however, provide the greatest gains over existing capability at temperate sites. This is because the reduction in sky brightness occurs over the full, broadband pass of the windows.

5. At J (1.25 μm) and H (1.65 μm), where airglow emission dominates, typical sky fluxes are 300–600 μJy arcsec^{-2} and 600–1500 μJy arcsec^{-2}, respectively, or one-third and one-half the corresponding fluxes at Siding Spring. At K (2.2 μm) the typical background is 300–700 μJy arcsec^{-2}, approximately 10% the flux in the K_n (2.1 μm) window at Siding Spring. However the reduction here can be attributed mostly to decreased thermal, rather than airglow, emission.

6. The H-band window is also somewhat wider, and cleaner, at the South Pole than at Siding Spring.

7. We find no evidence to suggest that auroral emission contributes in any significant way to the background in the $K_{\rm dark}$ window at the Pole.

8. During twilight, when the Sun is less than 10° below the horizon (and the height of the day/night terminator is

less than 100 km), scattered sunlight contributes to the sky background, particularly at shorter wavelengths. The intensity of the scattered background appears to be consistent with Rayleigh scattering, $1/\lambda^4$.

9. Scattered moonlight is also evident as a contributor to the sky brightness in the J band when the Moon is visible.

10. Visual estimates of cloud cover during winter, even by a trained observer, are unreliable at the Pole, especially during periods without moonlight.

We conclude that the South Pole offers significant reductions in the sky background, compared to temperate latitude observatories, across the entire near-IR waveband. The site holds the promise of providing significantly increased sensitivities, when using commensurate facilities, for observation of astronomical sources.

We are grateful for the efforts of many people in developing this site testing program at the South Pole. John Briggs nursed the IRPS through its first winter in 1994, and Bob Loewenstein and Bob Pernic oversaw much of the program. Matt Chamberlain has produced sky flux models that have proved invaluable for our interpretation. JACARA is the Joint Australian Centre for Astrophysical Research in Antarctica, a cooperative venture between the University of New South Wales and Australian National University. CARA is the Center for Astrophysical Research in Antarctica, an NSF Science and Technology center. This research was made possible by the award of a Small Grant from the Australian Research Council. The *COBE* data sets were developed by the NASA Goddard Space Flight Center under the guidance of the *COBE* Science Working Group and were provided by the NSSDC.

We gratefully acknowledge the efforts of A. T. Weatherwax and T. J. Rosenberg at the University of Maryland, L. J. Lanzerotti at Bell Labs, Lucent Technologies, and U. S. Inan at Stanford University for provision of the geophysical data used. This research was partially supported by the National Science Foundation under grants OPP-9505823 and 9529177 to the University of Maryland.

REFERENCES

Allen, D. A. 1981, Anglo-Australian Observatory User Guide UM-3 (AAO)
Ashley, M. C. B. 1998, in ASP Conf. Ser. 141, Astrophysics from Antarctica, ed. G. Novak & R. H. Landsberg (San Francisco: ASP), 285
Ashley, M. C. B., Burton, M. G., Lloyd, J. P., & Storey, J. W. V. 1995, Proc. SPIE, 2552, 33
Ashley, M. C. B., Burton, M. G., Storey, J. W. V., Bally, J., Briggs, J. W., Harper, D. A., & Lloyd, J. P. 1996, PASP, 108, 721
Barton, J. R., & Allen, D. A. 1980, PASP, 92, 368
Burton, M. G. 1998, in ASP Conf. Ser. 141, Astrophysics from Antarctica, ed. G. Novak & R. H. Landsberg (San Francisco: ASP), 3
Burton, M. G., Storey, J. W. V., & Ashley, M. C. B. 1999, Looking Deep in the Southern Sky, ed. R. Morganti & W. Couch (Berlin: Springer), 201
Burton, M. G., et al. 1994, Proc. Astron. Soc. Australia, 11, 127
Chamberlain, M., Burton, M. G., Storey, J. W. V., Ashley, M. C. B., & Harper, D. A. 1999, ApJ, submitted
Hahn, J. H., Warren, S. G., & London, J. 1985, J. Climate, 8, 1429
Harper, D. A. 1989, in AIP Conf. Proc. 198, Astrophysics in Antarctica, ed M. Pomerantz (New York: AIP), 123
Hauser, M. G., Kelsall, T., Leisawitz, D., & Weiland, J. L. 1998, *COBE* Diffuse Infrared Background Experiment (DIRBE) Explanatory Supplement, Version 2.3 (*COBE* Ref. Pub. 98-A; Greenbelt, MD: NASA/GSFC)
Loewenstein, R. F., Bero, C., Lloyd, J. P., Mrozek, F., Bally, J., & Theil, D. 1998, in ASP Conf. Ser. 141, Astrophysics from Antarctica, ed. G. Novak & R. H. Landsberg (San Francisco: ASP), 296
Mandolesi, N., et al. 1998, A&A, 331, 463
Marks, R. D., Vernin, J., Azouit, M., Briggs, J. W., Burton, M. G., Ashley, M. C. B., & Manigault, J. F. 1996, A&AS, 118, 385
Marks, R. D., Vernin, J., Azouit, M., Manigault, J. F., & Clevelin, C. 1999, A&A, 134, 161
Nguyen, H. T., Rauscher, B. J., Harper, D. A., Loewenstein, R. F., Pernic, R. J., Severson, S. A., & Hereld, M. 1996, PASP, 109, 718
Schneider, G., Paluzzi, P., & Oliver, J. P. 1989, J. Climate, 2, 295
Smith, C. H., & Harper, D. A. 1998, PASP, 110, 747
Storey, J. W. V., Ashley, M. C. B., & Burton, M. G. 1996, Publ. Astron. Soc. Australia, 13, 35
Wu, Q., & Rosenberg, T. J. 1992, Geophys. Res. Lett., 19, 69